

Supporting Information

Iron-doping-enhanced photoelectrochemical water splitting performance of nanostructured WO₃: A combined experimental and theoretical study

Teng Zhang^{ab}, Zonglong Zhu^{ab}, Haining Chen^b, Yang Bai^b, Shuang Xiao^{ab}, Xiaoli Zheng^b, Qingzhong Xue^c
Shihe Yang^{ab*}

Table. S1 The real concentration of Fe dopant in the prepared Fe-doped WO₃ Films

Element	Undoped WO ₃	2% Fe-doped WO ₃	5% Fe-doped WO ₃
Dopant content	0	1.21%	3.24%

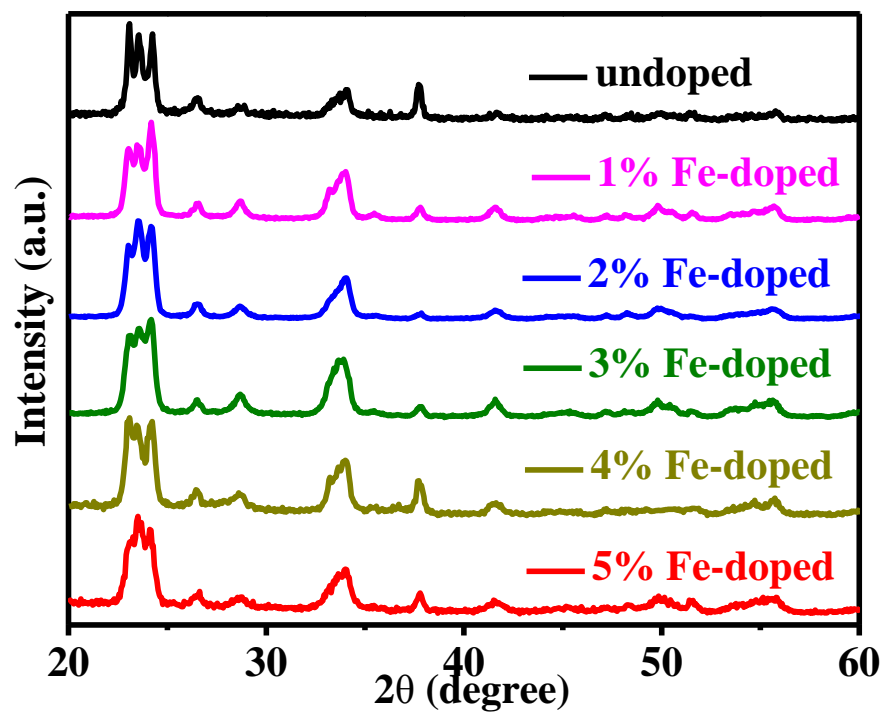


Fig. S1 XRD patterns of the prepared undoped and Fe-doped WO₃ films. All films have been annealed at 500 °C for 1 h.

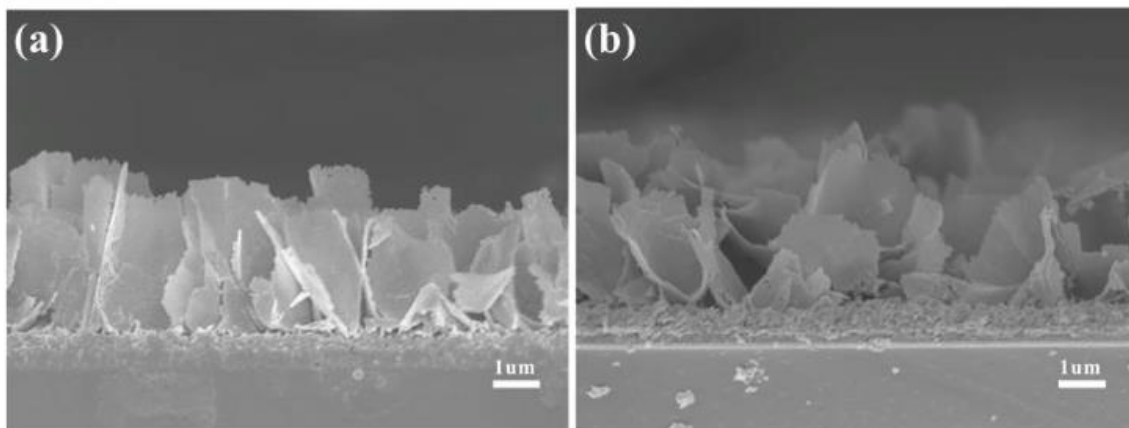


Fig. S2 SEM images recording the thickness of the undoped WO_3 (a) and 5% Fe-doped WO_3 (b) films grown on FTO glass.

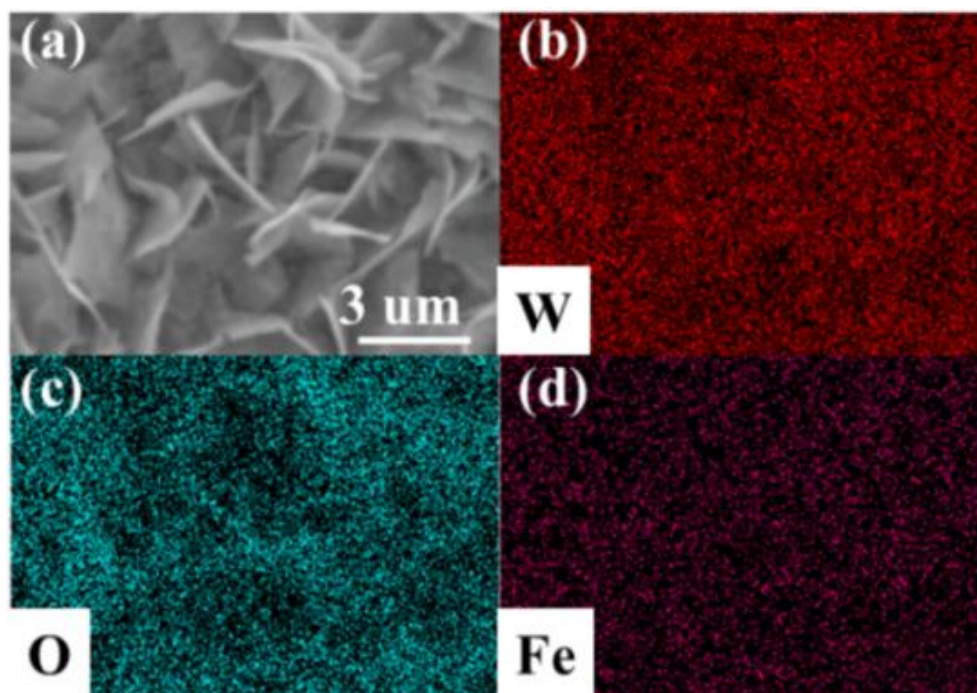


Fig. S3 Energy dispersive X-ray spectroscopy (EDS) of 2% Fe-doped WO_3 . (a) SEM image of the as-prepared 2% Fe-doped WO_3 , (b) W element map of the corresponding area in (a), (c) O element map of the area in (a), and (d) Fe map of the area in (a).

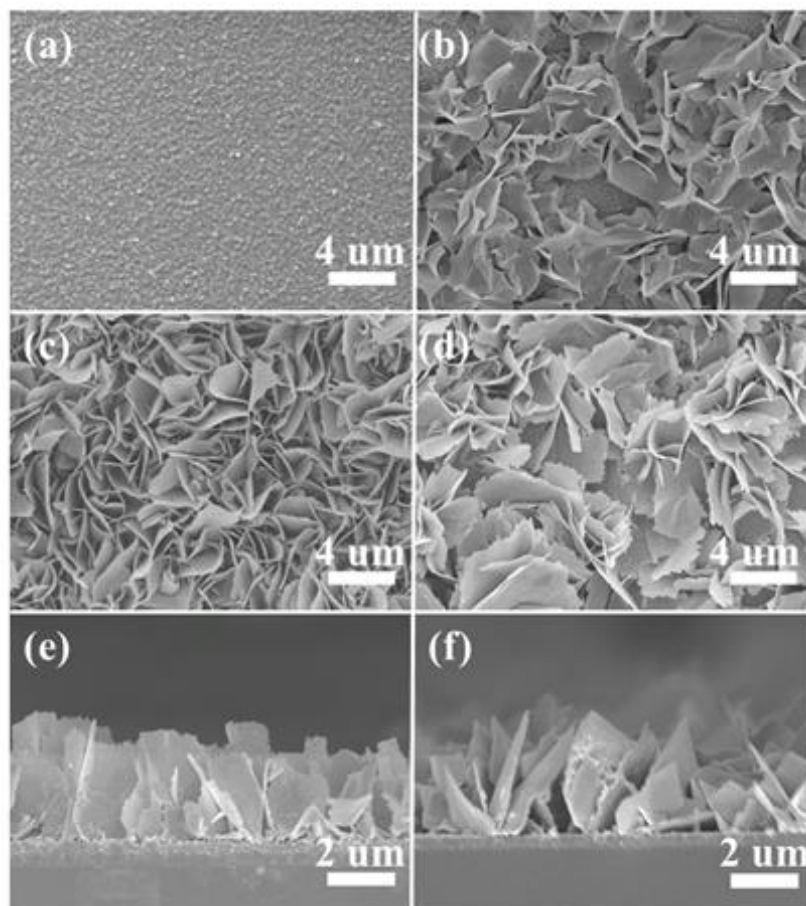


Fig. S4 Top-sectional SEM images of undoped WO_3 nanoflakes grown on FTO at 180°C for (a) 1, (b) 2, (c) 4 and (d) 6 h. Cross-sectional SEM images of undoped WO_3 nanoflakes grown on FTO for (e) 4 and (f) 6 h.

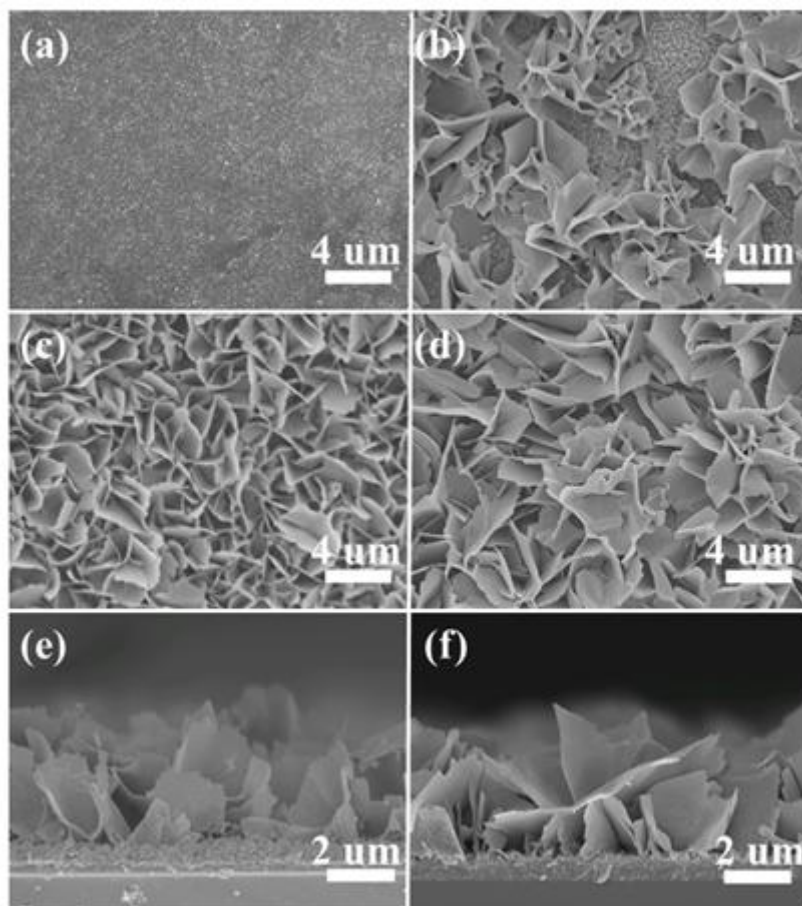


Fig. S5 Top-sectional SEM images of 5% Fe-doped WO_3 nanoflakes grown on FTO at 180°C for (a) 1, (b) 2, (c) 4 and (d) 6 h. Cross-sectional SEM images of the 5% Fe-doped WO_3 nanoflakes grown on FTO for (e) 4 and (f) 6 h.

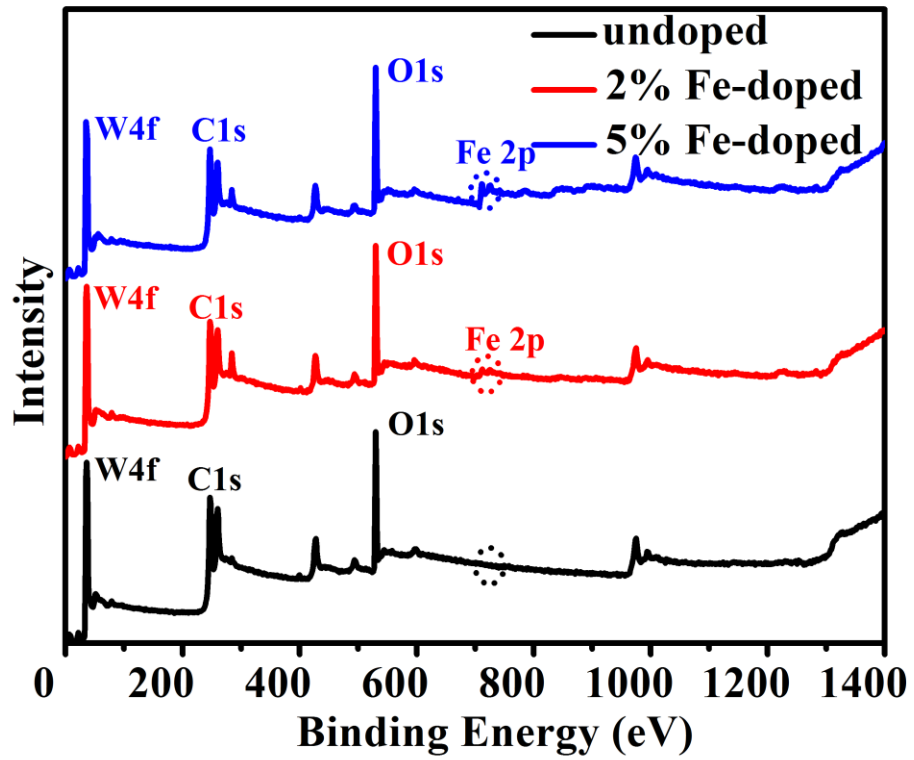


Fig. S6 XPS survey scans of the undoped, 2% and 5% Fe-doped nanostructured WO₃ films grown on FTO glass.

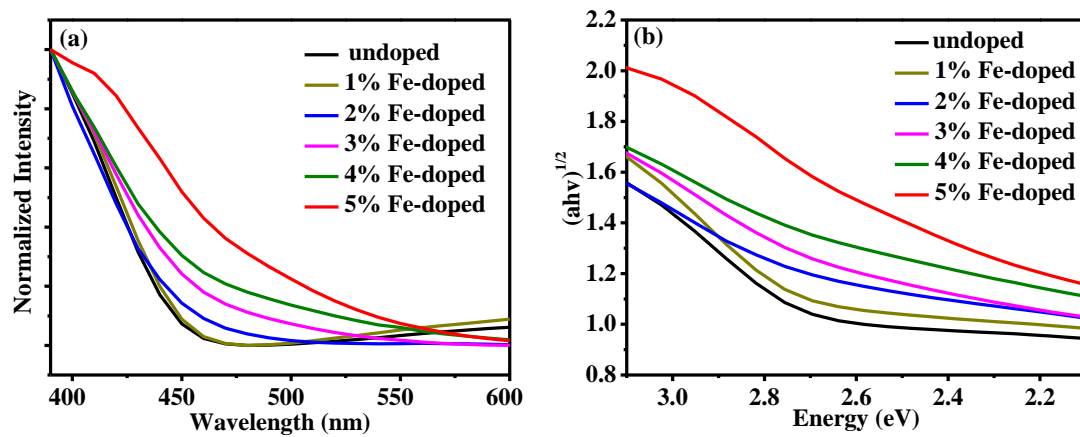


Fig. S7 (a) UV-vis adsorption spectra and (b) Tauc plots of the undoped WO₃ and Fe-doped WO₃ films.

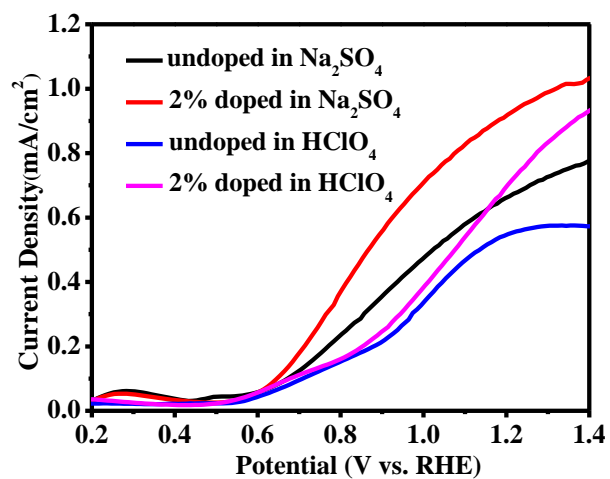


Fig. S8 Linear scan voltammograms of the undoped and 2% Fe-doped WO₃ in 0.1 mol/L Na₂SO₄ and 1 mol/L HClO₄ under AM1.5G simulated solar light (100 mWcm⁻²) with a scan rate of 10 mV s⁻¹.

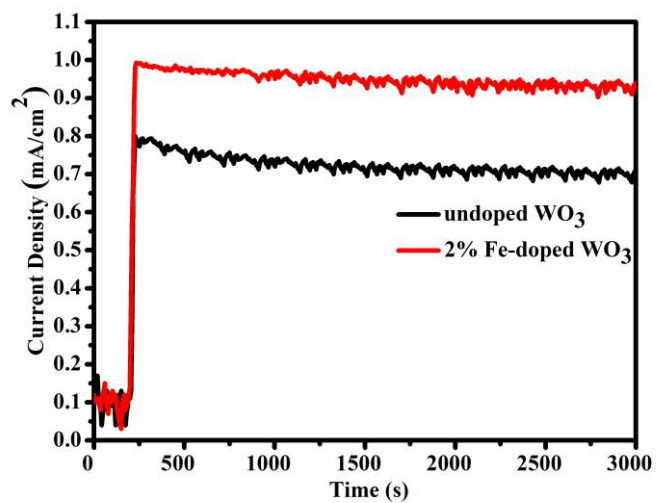


Fig. S9 The photocurrent vs. time curves of undoped WO₃ and 2% Fe-doped WO₃ collected at 1.23 V vs. RHE.

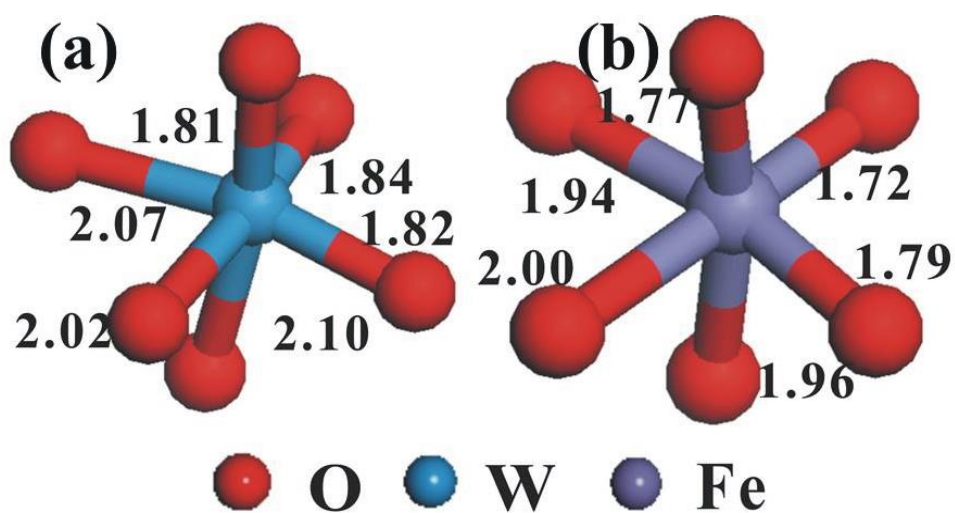


Fig. S10 Close-ups of the optimized bonding structures around the W (a) and Fe (b) atoms. The specific bonding lengths are indicated on the sides of the corresponding bonds.

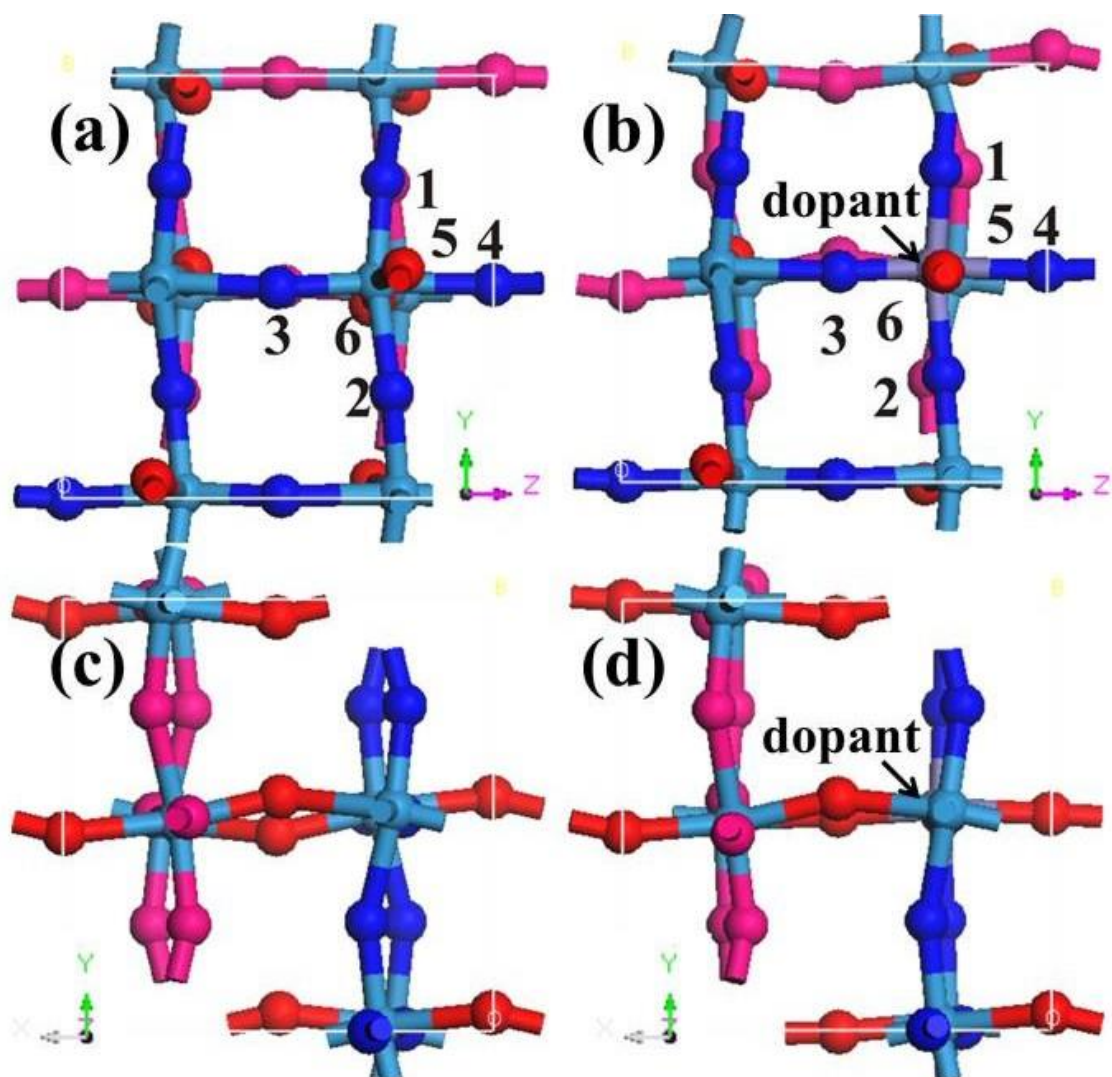


Fig. S11 Schematic showing the 6 independent oxygen vacancy sites in undoped WO_3 (a) and Fe-doped WO_3 (b) from the X direction. Schematic recording the morphologies of the undoped WO_3 (c) and Fe-doped WO_3 (d) from the Z direction. Here, the oxygen atoms in the first layer (dopant contained layer) have been marked by blue, while the underlayer oxygen atoms have been marked by pink, the indigo, purple and red balls represent the tungsten, iron dopant and the rest of the oxygen atoms.

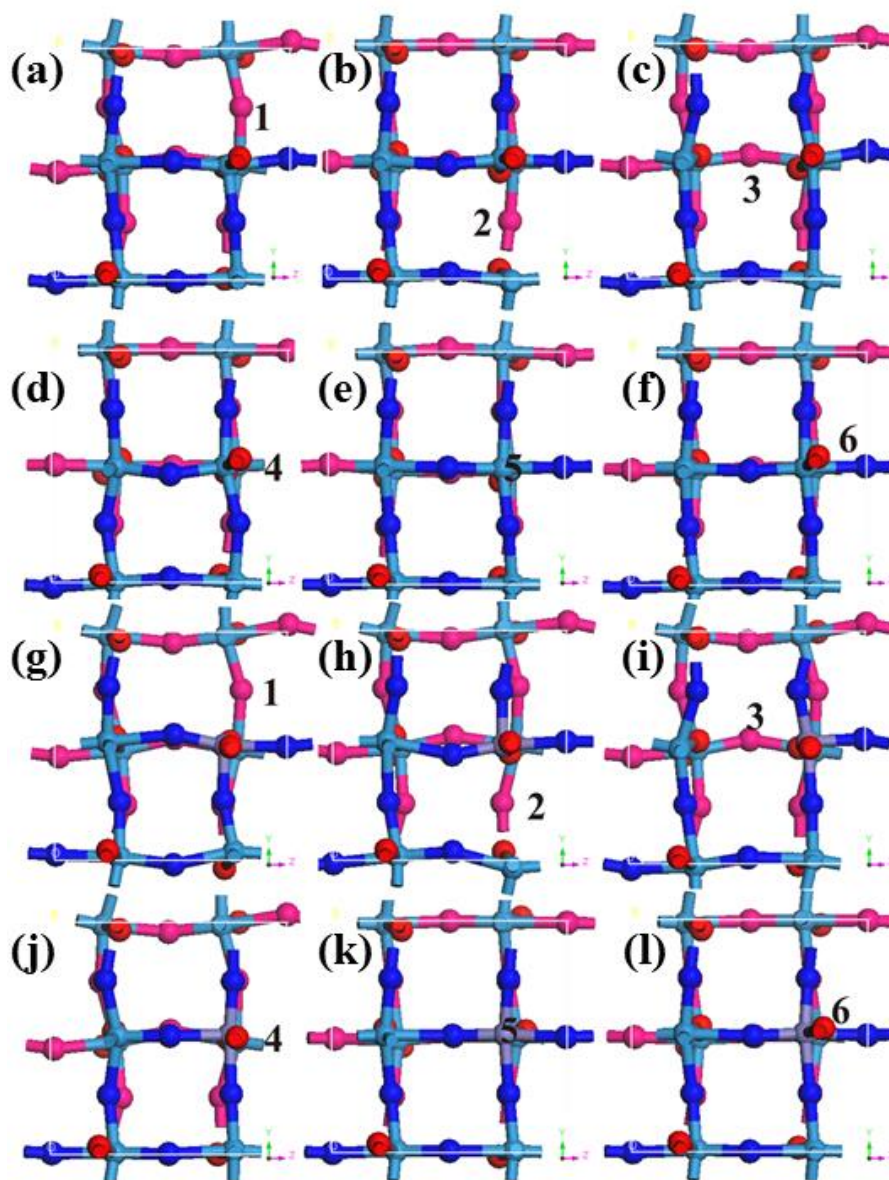


Fig. S12 The optimized geometries for the undoped WO_3 with an oxygen vacancy (a-f), and Fe-doped WO_3 with an oxygen vacancy (g-l). Here the positions of each oxygen vacancies are marked by the Arabic number. The oxygen atoms in the first layer (dopant contained layer) have been marked by blue, while the underlayer oxygen atoms have been marked by pink, the indigo, purple and red balls represent the tungsten, iron dopant and the rest of the oxygen atoms.